RESEARCH ARTICLE

NANO · MICRO small
www.small-journal.com

In Situ Carbon Thermal Reduction to Enrich Sulfur-Vacancy in Nickel Disulfide Cathode for Efficient Synthesizing Hydrogen Peroxide

Sijia Liu, Hao Ren, Fayou Tian, Lina Geng, Wangyang Cui, Jinhui Chen, Yan Lin, Mingbo Wu, and Zhongtao Li**

Transition metal catalysts are widely used in the 2e$^-$ ORR due to their cost-effectiveness. However, they often encounter issues related to low activity. Defect engineering are used on developing highly active catalysts, which can effectively modify active sites and promote electron transfer. Here, carbon-coated Ni_3S_2 (Ni_3S_2@C), where the additional sulfur vacancies (V_S) is prepared induced by the carbon layer is coupled with active nickel sites. Through in situ and ex situ experiments combined with DFT calculations, it is demonstrated that the carbon layer can regulate the quantity of V_S in Ni_3S_2. Materials with a higher concentration of V_S exhibit enhanced 2e$^-$ ORR activity and higher H_2O_2 selectivity. In situ Raman spectroscopy confirms that Ni serves as the key active site in this catalyst. DFT calculations indicate that the OOH binding energy (ΔG) decreases with an increase in the number of V_S, favoring the protonation of *OOH to generate H_2O_2. Upon performance testing, the average H_2O_2 selectivity is 92.3%, with the highest yield reaching up to 3860 mmol gcat^{-1} h^{-1}. It is noteworthy that Ni_3S_2@C exhibits high stability, with only a slight decrease in 2e$^-$ pathway selectivity after 5000 cycles of ADT.

1. Introduction

Hydrogen peroxide (H_2O_2), as an environmentally friendly and versatile high-efficiency green oxidant, has been widely applied in industries such as papermaking, chemical engineering, and sewage treatment.[1] Currently, H_2O_2 is manufactured via the anthraquinone process which has a number of disadvantages including non-distributed production, high-energy consumption, substantial organic by-product waste, and the need to transport the obtained H_2O_2 to the point-of-use.[2] To overcome these issues, the electrocatalytic 2e$^-$ ORR for the preparation of hydrogen peroxide has become an attractive strategy due to its safety, environmental and economic advantages.[3] Although there are numerous potential advantages to electrochemical H_2O_2 synthesis, the actual process is challenging because many electrode materials favor the competitive four-electron (4e$^-$) ORR to H_2O over the 2e$^-$ ORR to H_2O_2.[4] Therefore, it is essential to find ORR electrocatalysts with a high selectivity for H_2O_2 production via the 2e$^-$ pathway.[5]

Currently, enormous effort has been devoted to catalyst design for selective 2e$^-$ ORR production, including single-atom catalysts,[6] noble metal-based catalysts,[7] and carbon-based catalysts.[8] However, these materials still suffer from poor stability, scarcity, and low selectivity, respectively. Thus, it is important to develop abundant, highly active, and inexpensive transition metal (Ni, Co, Fe, etc.) catalysts for electrocatalytic ORR.[9] Among the transition metals, Ni has strong adsorption capabilities for atomic oxygen and molecular oxygen.[10] Moreover, Ni-based sulfides have received increasing attention due to their unique d-electron configuration and excellent conductivity.[11] Ni_3S_2, as a highly active phase in various NiSx (i.e. NiS, Ni_3S_2, NiS_2), exhibits excellent HER and OER electrocatalytic activity. However, it has rarely been explored in 2e$^-$ ORR.[12] The catalyst can be corroded by acidic or alkaline electrolytes. High overpotentials and interfaces in the liquid-solid catalytic system can lead to surface reconstruction of Ni_3S_2, which further contributes to the decrease in activity.[13] Additionally, the crystal structure of Ni_3S_2 consists partly of metal-nonmetal Ni—S bonds, resulting in hindered electron transfer, poor electrical conductivity, and electrocatalytic performance.[14] Therefore, maintaining the high stability of inorganic catalysts, especially non-noble transition metal catalysts, without sacrificing their activity under appropriate reaction conditions remains a significant challenge.

Encapsulation of metals in carbon effectively prevents corrosion and reconstruction of active substances during the electrocatalytic reaction, thus maintaining high catalytic activity and

S. Liu, H. Ren, F. Tian, L. Geng, W. Cui, J. Chen, M. Wu, Z. Li
State Key Laboratory of Heavy Oil Processing
College of Chemical Engineering
China University of Petroleum (East China)
Qingdao 266580, P. R. China
E-mail: liztao@upc.edu.cn

Y. Lin
Department of Chemistry
Tsinghua University
Beijing 100084, P. R. China
E-mail: linyan@mail.tsinghua.edu.cn

The ORCID identification number(s) for the author(s) of this article can be found under https://doi.org/10.1002/smll.202405683

DOI: 10.1002/smll.202405683

stability.[15] Electrons are freely transferred between metal and carbon. There is an electronic interaction between metal and carbon materials. The intermolecular charge transfer effect can modulate the catalyst charge state and further regulate the electrocatalytic activity.[16] Wang et al. demonstrated that a carbon layer can protect the catalyst and enhance its conductivity, ensuring that electrons transfer promptly to reactants, thereby avoiding over-accumulation of electrons, self-reduction leading to structural collapse, and subsequent performance decline.[15b] Additionally, a high-temperature carbon layer has a positive effect on defect formation. Vacancies in the catalyst can synergize with nearby active metals to modulate the intrinsic electronic structure of the catalyst. This can alter the binding strength of the active species to O_2 and intermediates, thereby significantly suppressing the cleavage of the O—O bond in the *OOH intermediate and thus led to an increase in $2e^-$ selectivity.[17]

Here, we synthesized a Ni-based sulfide catalyst with S vacancies encapsulated in a carbon layer (Ni_3S_2@C) through simultaneous CVD chemical vapor deposition and high-temperature annealing, and investigated the mechanism of the impact of its composite structure on the alkaline $2e^-$ ORR reaction pathway. Electrochemical tests showed that Ni_3S_2@C exhibits excellent $2e^-$ oxygen reduction selectivity, with the highest H_2O_2 selectivity reaching 93.7%. When Ni_3S_2@C was used as a catalyst for assembling an H-cell and a flow cell to produce H_2O_2, the H_2O_2 yields were 435 and 3860 mmol $gcat^{-1}$ h^{-1}, respectively. Furthermore, this catalyst was able to maintain its excellent working efficiency for 43200s, as well as 5000 CV cycles. The experimental results show that the Ni_3S_2@C catalyst induces more V_S through high-temperature induction of the carbon layer, promoting *OOH formation. The carbon layer enhances conductivity and increases the internal Ni electron density while slowing down the corrosion of electrons on the catalyst. The excellent reactivity was attributed to the increased V_S of the CVD-coated carbon layer, and in situ characterization demonstrated that this structure reduced the reaction voltage. This further improved the reaction kinetics and facilitated the production of H_2O_2 by protonation of *OOH.

2. Results and Discussions

2.1. Morphology and Structure Characterization

Nano carbon-encapsulated transition metal inorganic catalysts were prepared using high-temperature annealing and in-situ chemical vapor deposition (Figure S1, Supporting Information). The samples were denoted as Ni_3S_2@C, while those subjected to only 600°C calcination were denoted as NiS_2-600. The samples of carbon black treated by CVD are noted as CB@C. To explore the optimal performance, different calcination temperatures and anhydrous ethanol feed amounts were adjusted (experimental part of the supporting information), and the synthesized Ni_3S_2@C were all prepared under optimal reaction conditions. The synthesis process and microscopic reaction mechanisms of Ni_3S_2@C with sulfur vacancies (V_S) are illustrated in **Figure 1a**. The scanning electron microscope (SEM) image showed that the precursor NiS_2 was a microsphere composed of nanosheets with various sizes. The thickness of the initial nanosheets is ≈30 nm and the surface is relatively smooth (Figure S2a, Supporting Information). NiS_2 lost its nanosheet structure after 600°C high temperature (Figure S2b, Supporting Information). The SEM image showed that the microspheres of Ni_3S_2@C disappeared after carbon coating, and a network of loose and rough carbon layers appeared on the surface. The deposited carbon layer significantly changed the smooth and intact surface of NiS_2 and NiS_2-600, which resulted in more exposed sites and surface area for Ni_3S_2@C compared to NiS_2 and NiS_2-600, conducive to the ORR process (Figure 1b). The specific surface area and pore size distribution of Ni_3S_2@C and NiS_2-600 were next further analyzed by performing adsorption and desorption tests under nitrogen conditions. The specific surface areas of the two materials were calculated to be 333 and 100 m^2 g^{-1}, respectively. The specific surface area of Ni_3S_2@C is greater than that of NiS_2-600 due to the surface roughness of the carbon layer carbon layer increases the contact area(Figure S3, Supporting Information). The high-resolution transmission electron microscopy (HRTEM) image (the inset in Figure 1c) distinctly showed the lattice fringes with a spacing of 0.287 nm, corresponding to the (110) plane of Ni_3S_2. This indicates that NiS_2 is successfully transformed into Ni_3S_2 after CVD deposition (Figure 1c). Transmission electron microscopy (TEM) clearly showed that Ni_3S_2 nanoparticles were encapsulated with a layer of carbon on the outer layer (Figure S4, Supporting Information). TEM mapping showed that the elements are uniformly distributed in the material (Figure 1d). Furthermore, XRD results showed that the precursor nickel disulfide was successfully converted to Ni_3S_2 after calcination at 600°C. In addition to the diffraction peaks of Ni_3S_2, the diffraction peaks of the amorphous carbon (002) crystal surface appeared at $2\theta = 25.073°$ in the CVD deposited material. This above proof suggests that the inner catalyst is still Ni_3S_2 after the CVD deposition and the carbon layer is successfully covered on the surface (Figure 1e). In addition, Raman spectroscopy showed two characteristic peaks at 278.9 and 476.4 cm^{-1} for the precursor, corresponding to the Eg and Ag phonons of NiS_2, further confirming the successful synthesis of the precursor NiS_2 (Figure S5, Supporting Information). The Raman spectrum of NiS_2-600 showed characteristic peaks at 185.4, 324.2, 198.1, 222.2, 305.7, and 349.0 cm^{-1}, corresponding to two A_1 and four E vibrational modes of Ni_3S_2, indicating that NiS_2 transformed into the Ni_3S_2 phase after direct calcination at 600°C (Figure 1f). The Raman spectrum of Ni_3S_2@C showed only D and G peaks of carbon at 1340 and 1587 cm^{-1}, and characteristic peaks of Ni_3S_2 were not found. This is because Raman spectroscopy is a surface analysis method, whereas Ni_3S_2@C is covered with a porous carbon layer, so only D and G peaks appear in its Raman plot. (Figure 1g). In summary, SEM and TEM characterization confirmed the morphology of Ni_3S_2@C and its encapsulation by a carbon layer, while XRD and Raman tests demonstrated the successful synthesis of the Ni_3S_2@C material.

Furthermore, to investigate the effect of the electronic environment of the catalyst on the ORR reaction, X-ray photoelectron spectroscopy (XPS) is used to analyze the composition and valence states of the elements in the materials. The XPS spectrum showed that the catalyst is mainly composed of four elements, S, C, O, and Ni (Figure S6, Supporting Information). The Ni_3S_2@C catalyst exhibited a high carbon content of 91.89% (Table S1, Supporting Information), indicating that the porous amorphous carbon was successfully encapsulated on the surface of the material. Apparently, the high-resolution Ni $2p_{3/2}$ and $2p_{1/2}$ XPS spectrum

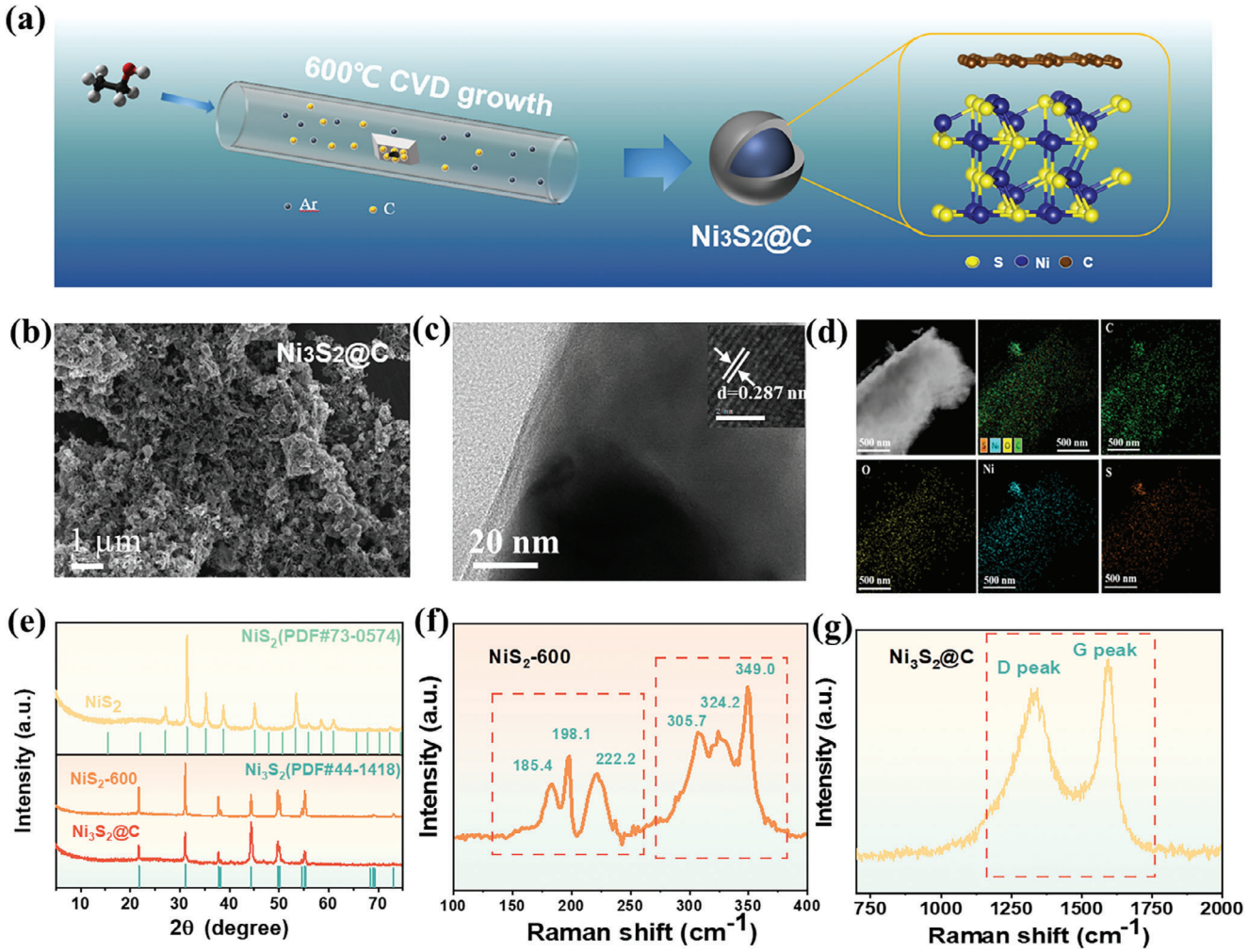

Figure 1. Morphology and structural characterization. a) Schematic diagram of the formation of defect-rich Ni_3S_2@C. b) SEM images Ni_3S_2@C catalysts. c) HRTEM images and d) Mapping of Ni_3S_2@C. e)XRD pattern of NiS_2, NiS_2-600, and Ni_3S_2@C catalysts. Raman spectra of f) NiS_2-600 and g) Ni_3S_2@C catalysts.

for Ni_3S_2@C shifted to the lower binding energy as compared to that of NiS_2-600(**Figure 2a**). The area ratio of low-valent Ni in Ni_3S_2@C was larger than that of NiS_2-600. These two signs implied that the valence state of Ni was reduced in the presence of a carbon layer, demonstrating the existence of an electronic interaction between the CVD-deposited carbon layer and the inner catalyst. During the reaction, this interaction maintained the Ni active site in an electron-rich state, increasing its reactivity.[18] To further demonstrate the advantageous role played by the carbon layer for charge transfer, we perform differential charge simulations with or without covering the carbon layer (Figure S7, Supporting Information). Yellow represents electron aggregation and blue represents electron deletion. The presence of a large blue color in the carbon layer and a large yellow colour below the carbon layer demonstrates the efficient transfer of electrons from the carbon layer to the inner catalyst. In addition, the comparison of high-resolution S 2p XPS spectra for NiS_2-600 and Ni_3S_2@C also revealed the decrease in the valence state of S and the introduction of S vacancies (Figure 2b). Furthermore, a C-S-C peak appeared at 164.56 eV in Ni_3S_2@C, suggesting the existence of a porous carbon layer on the surface of Ni_3S_2. In order to compare the difference between the CVD deposited carbon and the conventional cladding carbon, glucose and precursor NiS_2 were co-calcined to form the sample Ni_3S_2-Glu@C. The Ni 2p spectrum of Ni_3S_2-Glu@C showed that the binding energy of Ni $2p_{3/2}$ and Ni $2p_{1/2}$ were the same as that of NiS_2-600 (Figure 2c), whereas the binding energy of Ni_3S_2@C was shifted to lower binding energy. This demonstrated that the CVD-coated carbon layer possessed the ability to electronically modulate and lower the inner Ni valence state, which was not available with conventional annealing thermal synthesis methods. The electron paramagnetic resonance (EPR) signal (Figure 2d) at g = 2.003 was ascribed to the formation of S vacancies, with higher EPR signal intensity indicating more concentrated S vacancies.[19] The higher intensity of the Ni_3S_2@C signal indicated the high V_S concentration, while faint V_S were present in CB@C.[20] This is because the carbon layer deposited by CVD has a certain reduction effect at high temperatures, effectively promoting the formation of vacancies. Defect vacancies and active material Ni_3S_2 have a strong interaction, reducing the reaction energy barrier of ORR. In

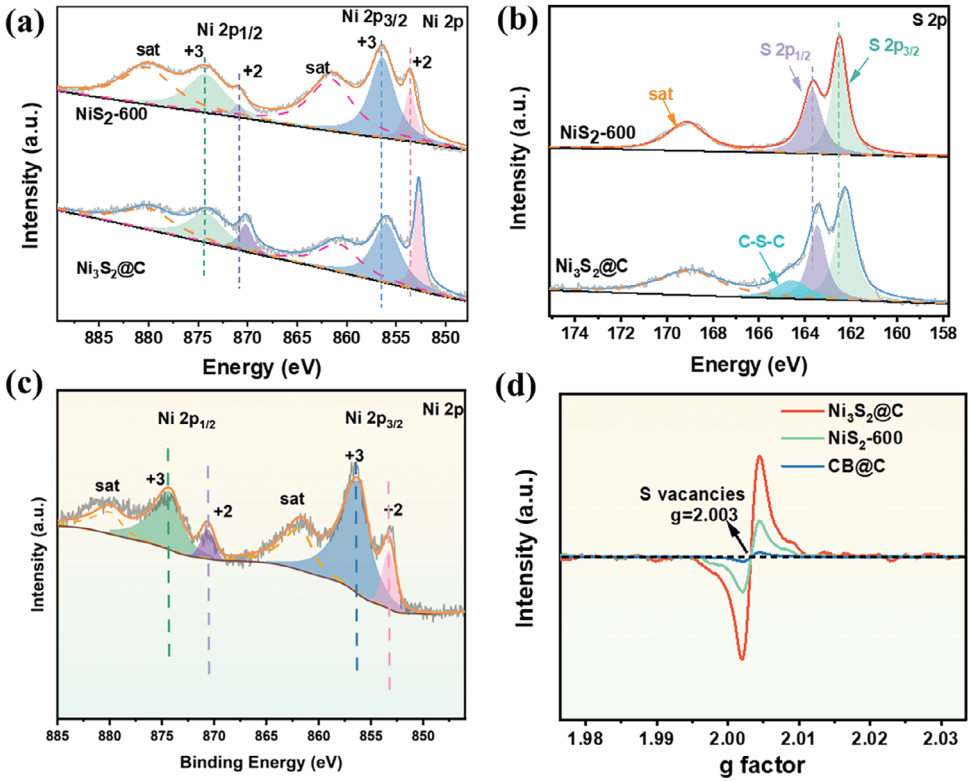

Figure 2. XPS characterization of different samples is used to study chemical valence. a) High-resolution Ni 2p XPS of NiS_2-600 and Ni_3S_2@C. b) High-resolution S 2p XPS of NiS_2-600 and Ni_3S_2@C. c) High-resolution Ni 2p XPS of Ni_3S_2-Glu@C. d) EPR spectra of NiS_2-600 CB@C and Ni_3S_2@C.

conclusion, the carbon layer deposited via CVD modulates the electronic structure of Ni_3S_2 and synergistically interacts with vacancies to lower the energy barrier of the 2e⁻ ORR pathway.

2.2. Electrocatalytic Performance of Catalysts

To investigate the effect of the above catalyst structural changes on the ORR performance, the electrocatalytic activity of all samples (NiS_2, NiS_2-600, Ni_3S_2@C, and CB@C) was evaluated using rotating ring-disk electrode (RRDE) in 0.1 M KOH electrolyte. From the cyclic voltammetry (CV) curves, it can be observed that Ni_3S_2@C showed an oxygen reduction peak at 0.574 V under saturated O_2 atmosphere, which was not observed under saturated Ar. This is an indication that Ni_3S_2@C has excellent catalytic activity for ORR (Figure S9, Supporting Information). From the cyclic voltammetry curves of different catalysts in a saturated O_2 atmosphere (Figure S10, Supporting Information), it can be seen that Ni_3S_2@C has the strongest catalytic activity compared to NiS_2-600 and CB@C, respectively. From the linear scanning voltammetry (LSV) curve, Ni_3S_2@C exhibits the highest ring current density (**Figure** 3a,d). This is attributed to the fact that the surface of Ni_3S_2@C is coated with a carbon layer, which can improve the electrical conductivity of the material, thereby increasing the limiting current. The electron transfer number (Figure 3b) and H_2O_2 selectivity (Figure 3c) of different materials at 0.165 V≈0.5 V vs. RHE were used to assess the catalytic performance. The average electron transfer number of NiS_2 was 2.81, and the highest H_2O_2 selectivity was only 66.9%. On the other hand, the average electron transfer number of NiS_2-600 was 2.26 and the average H_2O_2 selectivity was 89.3%. The 2e⁻ ORR selectivity of NiS_2-600 is much better than that of NiS_e, which is due to the conversion of NiS_2 phase to Ni_3S_2 phase. Compared with NiS_2-600, the average electron transfer number of Ni_3S_2@C was reduced to 2.18, which was closer to 2. The H_2O_2 selectivity averaged 92.3% and remained above 90% over a wide voltage range. The result suggests that Ni_3S_2@C prefers the 2e⁻ ORR pathway. This is attributed to the synergistic interaction between the CVD-deposited carbon layer and the internal Ni, which effectively modulates the electron density around Ni and the concentration of V_S The average electron transfer number of CB@C in the voltage range of 0.165–0.5 V was 2.88, and the highest H_2O_2 selectivity was only 66.6%. The performance of CB@C is much inferior to that of NiS_2-600 and Ni_3S_2@C, suggesting that the Ni_3S_2 crystalline phase is the main source of 2e⁻ ORR activity. To further explore the ORR catalytic activity, measurements of the double-layer capacitance (C_{dl}) of the electrode were conducted to evaluate the effective electrochemical active surface area (ECSA) (Figure 3e). Based on CV curves in Figure S16 (Supporting Information), the C_{dl} values of Ni_3S_2@C and NiS_2-600 were calculated to be $9.998*10^{-1}$ and $3.335*10^{-1}$ mF cm^{-2} from the slope of the linear fit, respectively (non-Faradaic process), indicating that Ni_3S_2@C exposed more accessible active sites. Based on the C_{dl} values, the ECSA values for Ni_3S_2@C and NiS_2-600 were estimated to be 24.9 and 8.3 cm^{-2}, respectively. Furthermore, Ni_3S_2@C had the smallest Tafel slope of 79.58 mV dec^{-1},

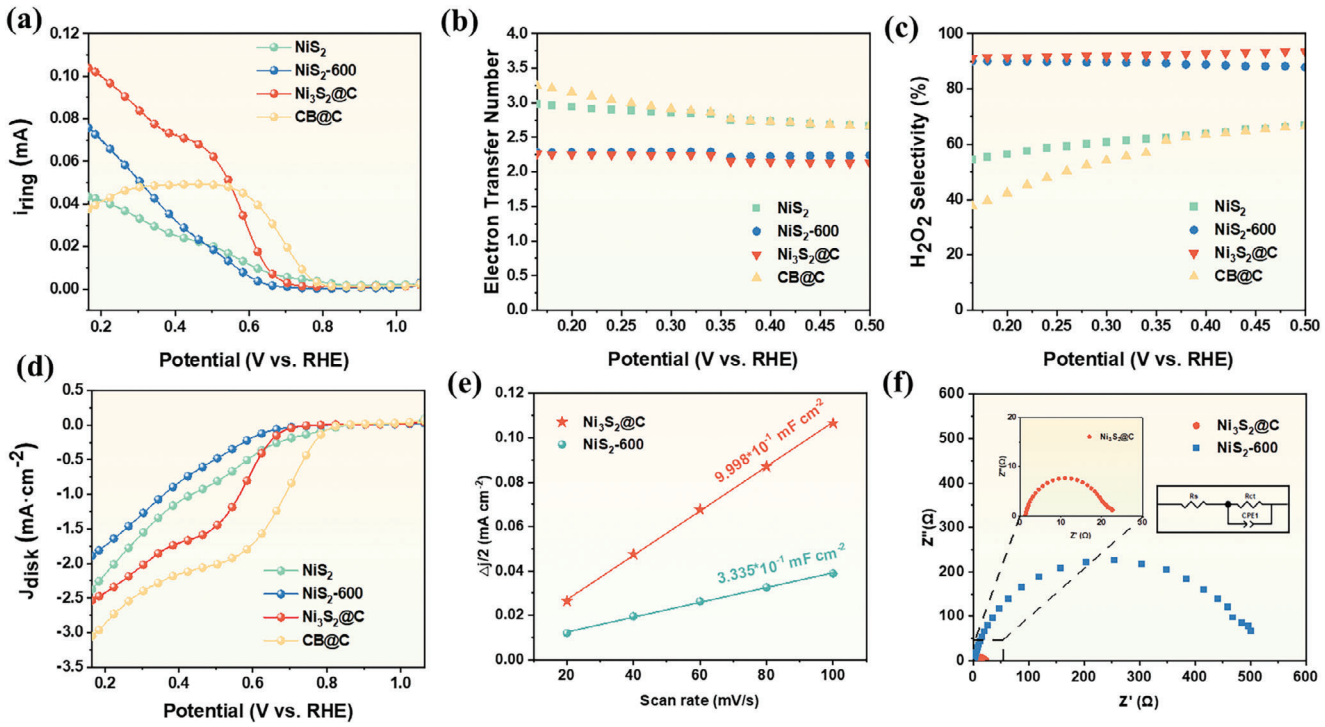

Figure 3. Electrochemical test. a) disk current density, b) electron transfer number of individual O_2 molecule, c) H_2O_2 selectivity and d) ring current of NiS_2, NiS_2-600, Ni_3S_2@Cand CB@C catalysts obtained by RRDE testing. e) Double-layer capacitance (C_{dl}) for NiS_2-600 and Ni_3S_2@C, f) EIS curves of NiS_2-600 and Ni_3S_2@C (The equivalent circuit is shown in the inset).

outperforming NiS_2, NiS_2-600, and CB@C (282.26, 133.71, and 131.65 mV dec^{-1}, respectively) (Figure S17, Supporting Information), which indicated that the ORR kinetics of the catalyst with carbon layer and V_S is considerably improved. Moreover, electrochemical impedance spectroscopy (EIS) was employed to further evaluate the reaction kinetics on catalysts. The Nyquist plot was fitted using an equivalent circuit (the inset in Figure 3f), and the charge transfer resistance (R_{ct}) of Ni_3S_2@C was 21.17 Ω, much lower than that of untreated NiS_2-600. The results confirm that the carbon layer can significantly improve the electrical conductivity of the catalyst.

The properties of Ni_3S_2@C for the production of hydrogen peroxide were investigated by electrolysis experiments with different reaction devices. After reacting for 1800 s under a current density of -50 mA cm^{-2} (**Figure 4a**), the H_2O_2 yield was 435 mmol $gcat^{-1}$ h^{-1} (Figure S18, Supporting Information). The production rate of H_2O_2 in the H-cell is still limited by mass transfer. In order to reduce the mass transfer limitation and further improve the H_2O_2 yield, a three-phase flow reactor was used (Figure 4b, the inset in Figure 4b showed a schematic diagram of the flow cell reaction setup). The H_2O_2 yield in the flow reactor was 3860 mmol $gcat^{-1}$ h^{-1} (Figure S19, Supporting Information), which far exceeds that in the H-cell. In addition, stability tests at 0.5 V disk voltage and 1.2 V ring voltage showed that the currents of the disk and ring remained stable within 12 h, indicating that Ni_3S_2@C has good electrocatalytic stability for ORR (Figure 4c). It is worth noting that Ni_3S_2@C exhibits better performance compared to reported advanced metal-based electrocatalysts (Figure 4d; Table S2, Supporting Information).

In order to further demonstrate the structural stability of the catalyst, the morphology and electrochemical performance of the samples were analyzed after conducting 5000 cycles of accelerated durability testing (ADT) experiments.[18b] SEM showed that the initial structure of NiS_2-600 was destroyed by current and electrolyte, exhibiting that the initial structure was reconstructed into smaller coral-like microspheres after electrolysis. In contrast, a small portion of the carbon layer of Ni_3S_2@C was corroded by the electrolyte, exposing the Ni_3S_2 microsphere structure without abnormal changes in morphology (Figure S20, Supporting Information). This further confirmed the protective effect of Ni_3S_2@C on the inner catalyst. The electron transfer coefficient increased from 2.18 to ≈2.5. Hydrogen peroxide selectivity decreased slightly but remained at ≈90% (Figure S21, Supporting Information). This further confirms the stability and excellent electrochemical performance of Ni_3S_2@C.

2.3. Exploration of Catalytic Mechanism

In-suit EIS recorded at various potentials was utilized to track the electrochemical processes of ORR (**Figure 5a**). The Bode phase plots of the catalyst presented a maximum characteristic frequency (ωp) in the frequency range of 0.1–100 Hz. As the applied potential decreases from 0.764 to 0.364 V, the phase angle of ωp gradually decreased, while the peak center shifted towards the high-frequency side.[9c] In this case, the decrease in ωp was faster for Ni_3S_2@C, while the decrease was slower for NiS_2-600, with a significantly smaller magnitude of peak

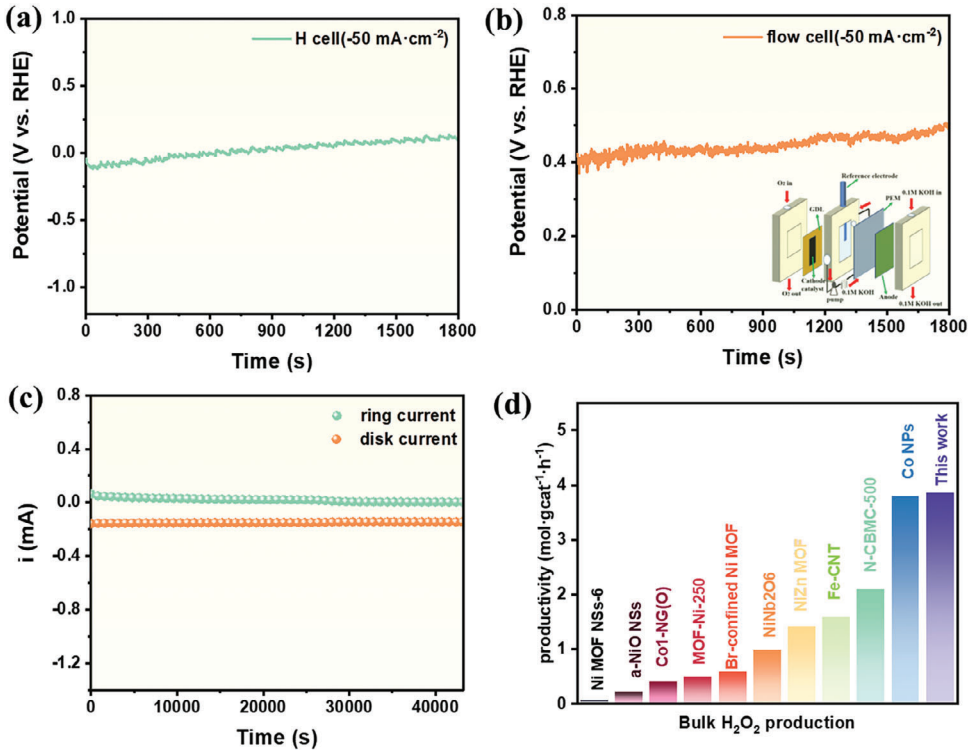

Figure 4. Catalytic performance. Electrolysis curves of Ni_3S_2@Ccatalyst in a) H-cell and b) flow cell at the current density of -50 mA cm^{-2}, The small picture in the figure is the schematic diagram of the device. c) Stability performance of Ni_3S_2@C catalyst. d) Comparison of bulk H_2O_2 production of Ni_3S_2@C with previously reported electrocatalysts.

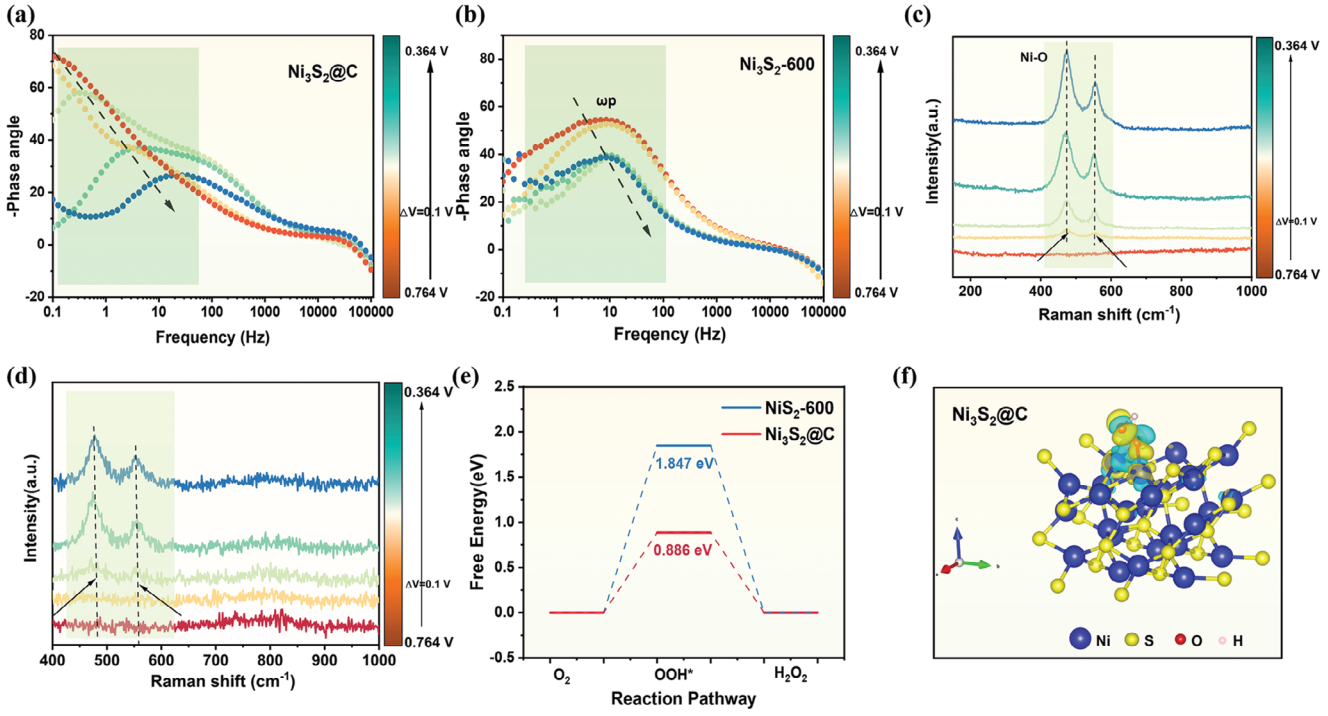

Figure 5. In situ experiments and DFT calculations. In situ electrochemical impedance spectroscopy of a) Ni_3S_2@C and b) NiS_2-600. In situ Raman spectra of c) Ni_3S_2@C and d) NiS_2-600. e) Free energy diagram for $2e^-$ ORR at 0.70 V for all models. f) Differential charge density plot of Ni_3S_2@C.

variation (Figure 5b). This indicates accelerated electron transfer behavior and improved surface reaction kinetics of *OOH intermediates for Ni_3S_2@C, further facilitating the occurrence of the 2e⁻ pathway ORR.[15a]

To further investigate the catalytic mechanism in the ORR process, in-situ Raman spectroscopy was performed on Ni_3S_2@C in 0.1 M KOH (0.764–0.364 V vs RHE) with a voltage interval of 0.1 V (Figure 5c). The peaks at 472 and 552 cm^{-1} emerged when the reduction potential exceeded 0.664 V vs. RHE, which could be attributed to Ni—O bonds formed by adsorption of *OOH (* denotes catalytic site) on Ni_3S_2@C.[21] Relevant with the experimental conclusions, Ni served as the active site for the adsorption and desorption of *OOH in the 2e⁻ ORR process. As the ORR proceeded, the peak signals gradually increased and their wave numbers showed a slight shift compared to NiS_2-600. It is attributed to the higher concentration of V_S in Ni_3S_2@C that makes the adsorption of *OOH for Ni sites stronger. In comparison, similar peaks in NiS_2-600 appeared at 478and 552 cm^{-1} during ORR (Figure 5d), but the formation potential (0.564 V vs. RHE) was higher than that of Ni_3S_2@C, further demonstrating the superior performance of Ni_3S_2@C.

To further elucidate the role of V_S in the 2e⁻ ORR, Ni_3S_2 with varying V_S concentrations and their corresponding pristine counterparts were synthesized (Figure S22, Supporting Information). The Gibbs free energy (ΔG) of the 2e⁻ ORR was calculated using density functional theory (DFT) and plotted at the ORR equilibrium potential (U = 0.74 V). The catalytic process of 2e⁻ ORR in alkaline electrolytes is governed by the following elementary reactions.[22]

$$O_2 + * + H_2O + e^- \rightarrow OOH^* + OH^- \quad (1)$$

$$OOH^* + e^- \rightarrow HO_2^- + * \quad (2)$$

In step (1), the ΔG for Ni_3S_2@C was 0.886 eV, while NiS_2-600 was 1.874 eV (Figure 5e; Table S3, Supporting Information). The ΔG decreased with the presence of more V_S, indicating that Ni_3S_2@C facilitates the protonation of *OOH to generate H_2O_2. The Ni_3S_2@C surface with a higher concentration of V_S exhibited high activity for the formation of H_2O_2. Density Functional Theory (DFT) calculations were used to compare the changes in $\Delta E_{ads}(O_2)$ values in Ni_3S_2@C and NiS_2-600 (Figure S23, Supporting Information). Ni_3S_2@C has an oxygen adsorption energy of −0.97 eV, while NiS_2-600 is −0.44 eV. Simply in terms, a more negative $\Delta E_{ads}(O_2)$ value means a higher saturation coverage of oxygen on the substrate. Therefore, Ni_3S_2@C has superior oxygen adsorption capacity. For the oxygen reduction reaction, Ni_3S_2@C performs better than NiS_2-600. Furthermore, the differential charge density distribution between the adsorbed *OOH and the catalyst substrates (Ni_3S_2@C and NiS_2-600) was also simulated (Figure 5f; Figure S24, Supporting Information). Yellow and Cyan blue represent electron aggregation and deletion, respectively. By comparing the electronic distribution behaviors of Ni_3S_2@C and NiS_2-600, it can be observed that the electrons of *OOH in Ni_3S_2@C were redistributed. There was a more pronounced charge localization between the adsorbed *OOH and Ni_3S_2@C, further enhancing the binding of the active site to the active intermediate, thus facilitating the 2e⁻ ORR pathway.

3. Conclusions

Ni_3S_2 nano catalyst with a CVD-deposited carbon layer (Ni_3S_2@C) was developed and demonstrated to be a highly active and selective catalyst for H_2O_2 production in alkaline electrolytes. The prepared Ni_3S_2@C showed excellent 2e⁻ ORR catalytic activity, with the highest H_2O_2 selectivity reaching 93.7%. The H_2O_2 yield was 435 and 3860 mmol $gcat^{-1}$ h^{-1} in the H-cell and flow cell, respectively. The experimental results showed that the CVD carbon coating produced more V_S, while regulating the electron density of Ni in Ni_3S_2. In situ characterization combined with calculations demonstrated that a high concentration of V_S reduced the onset potential, optimized the free energy of *OOH intermediates and inhibited the competitive 4e⁻ ORR pathway for selective H_2O_2 production. In addition, the outer encapsulation structure of multilayer carbon slowed down the dissolution of Ni_3S_2 in the electrolyte and ensured the stability of the catalyst. Therefore, the Ni_3S_2@C composite is a promising material for preparing H_2O_2 electrocatalysts via the 2e⁻ ORR.

4. Experimental Section

Catalyst preparation: 0.01 mol of $NiSO_4{\cdot}6H_2O$, 0.01 mol of $Na_2S_2O_3{\cdot}5H_2O$, and 0.01 mol of sublimed sulfur were dissolved in a beaker containing 40 mL of deionized water. After ultrasonication, the mixture was hydrothermally treated at 140°C for 24 h. Subsequently, the resulting product was sequentially washed with anhydrous ethanol, CS_2, 1 M HCl, and deionized water to remove residual sublimed sulfur and impurities. Finally, the NiS_2 precursor was obtained by vacuum drying at 80°C for 10 h. 100 mg of NiS_2 powder was placed on a tubular furnace connected to a CVD generator and annealed at 600°C for 2 h under argon protection. During the annealing process, when the temperature reached 560°C, the gas-phase generator and heating switch were turned on to introduce anhydrous ethanol into the gas-phase generator. Once the sample volume reached 40 mL, the gas-phase generator was turned off. Ni_3S_2@C was obtained after the tubular furnace heating program was completed and cooled to room temperature. The chemical vapor deposition step was omitted for NiS_2-600.

Catalyst characterization: The synthesized samples were characterized using various analytical techniques. Scanning electron microscope (SEM) images were acquired on a ZEISS Gemini 300 scanning electron microscope operating at an accelerating voltage of 1.5 kV. Transmission electron microscopy (TEM) and high-resolution TEM (HRTEM) were conducted on a JEOL-2100F (Japan) microscope operating at a voltage of 200 kV. The X-ray diffraction pattern was collected on a Bruker AXS D8 X-ray diffractometer with Cu K (= 1.54056 Å, 100 mA and 40 kV) under a scan rate of 5 degree min^{-1}. XPS spectra were firstly deoxygenated under Ar for 1 h and then investigated on a Thermo Scientific ESCALAB 250 XI spectroscopy equipped with an Al KX-ray source and the spectra were calibrated with a binding energy of 284.6 eV for C 1s. In- situ Raman was studied in an alkaline solution using a standard three-electrode system, where the synthetic electrocatalyst, Ag/AgCl electrode and platinum wire were used as working electrodes, reference electrode and counter electrode, respectively. In-situ Raman measurements were recorded from 0.764 to 0.364 V vs. RHE. with an interval of 0.1 V. In- situ EIS was tested on the Kooster work station using the same three-electrode system as above Raman (frequency voltage mode with frequency range of 10^5–10^{-1} Hz, voltage range of 0.764–0.364 V vs. RHE) and interval of 0.1 V.

Supporting Information

Supporting Information is available from the Wiley Online Library or from the author.

Acknowledgements

This work was supported by the National Key R&D Program of China (SQ2022YFE020274), National Natural Science Foundation of Shandong, China (ZR2021ZD24), the Financial Support from Taishan Scholar Project (tsqn201909062) and Fundamental Research Funds for Chinese Central Universities (27RA2304013).

Conflict of Interest

The authors declare no conflict of interest.

Author Contributions

Sijia Liu: Investigation, Writing – original draft. Hao Ren: Formal analysis. Fayou Tian: Formal analysis. Lina Geng: Investigation, Wangyang Cui: Investigation. Jinhui Chen: Investigation. Yan Lin: Writing – review & editing, Supervision. Mingbo Wu: Resources. Zhongtao Li: Conceptualization, Funding acquisition, Project administration.

Data Availability Statement

The data that support the findings of this study are available from the corresponding author upon reasonable request.

Keywords

electrocatalysts, hydrogen peroxide, oxygen reduction, transition metals, vacancy

Received: July 8, 2024
Revised: September 24, 2024
Published online:

[1] a) Y. Sun, L. Han, P. Strasser, *Chem. Soc. Rev.* **2020**, *49*, 6605; b) J. K. Edwards, B. Solsona, E. N. N, A. F. Carley, A. A. Herzing, C. J. Kiely, G. J. Hutchings, *Science* **2009**, *323*, 1037; c) J. W. F. To, J. W. D. Ng, S. Siahrostami, A. L. Koh, Y. Lee, Z. Chen, K. D. Fong, S. Chen, J. He, W. G. Bae, J. Wilcox, H. Y. Jeong, K. Kim, F. Studt, J. K. Nørskov, T. F. Jaramillo, Z. Bao, *Nano Res.* **2017**, *10*, 1163.

[2] a) J. M. Campos-Martin, G. Blanco-Brieva, J. L. G. Fierro, *Angew. Chem., Int. Ed.* **2006**, *45*, 6962; b) S. J. Freakley, Q. He, J. H. Harrhy, L. Lu, D. A. Crole, D. J. Morgan, E. N. Ntainjua, J. K. Edwards, A. F. Carley, A. Y. Borisevich, C. J. Kiely, G. J. Hutchings, *Science* **2016**, *351*, 965; c) S. Yang, A. Verdaguer-Casadevall, L. Arnarson, L. Silvioli, V. Čolić, R. Frydendal, J. Rossmeisl, I. Chorkendorff, I. E. L. Stephens, *ACS Catal.* **2018**, *8*, 4064.

[3] a) Y. Wang, G. I. N. Waterhouse, L. Shang, T. Zhang, *Adv. Energy Mater.* **2021**, *11*, 2003323; b) C. Ponce de León, *Nat. Catal.* **2020**, *3*, 96.

[4] a) Z. Lu, G. Chen, S. Siahrostami, Z. Chen, K. Liu, J. Xie, L. Liao, T. Wu, D. Lin, Y. Liu, T. F. Jaramillo, J. K. Nørskov, Y. Cui, *Nat. Catal.* **2018**, *1*, 156; b) J. Cheng, C. Lyu, H. Li, J. Wu, Y. Hu, B. Han, K. Wu, M. Hojamberdiev, D. Geng, *Appl. Catal., B* **2023**, *327*, 122470.

[5] L. Yan, P. Li, Q. Zhu, A. Kumar, K. Sun, S. Tian, X. Sun, *Chem* **2023**, *9*, 280.

[6] a) M. Song, W. Liu, J. Zhang, C. Zhang, X. Huang, D. Wang, *Adv. Funct. Mater.* **2023**, *33*, 2212087; b) M. Yan, Z. Wei, Z. Gong, B. Johannessen, G. Ye, G. He, J. Liu, S. Zhao, C. Cui, H. Fei, *Nat. Commun.* **2023**, *14*, 368.

[7] a) Q. Chang, P. Zhang, A. H. B. Mostaghimi, X. Zhao, S. R. Denny, J. H. Lee, H. Gao, Y. Zhang, H. L. Xin, S. Siahrostami, J. G. Chen, Z. Chen, *Nat. Commun.* **2020**, *11*, 2178; b) Z. Zheng, Y. H. Ng, D. W. Wang, R. Amal, *Adv. Mater.* **2016**, *28*, 9949.

[8] a) K. Lee, J. Lim, M. J. Lee, K. Ryu, H. Lee, J. Y. Kim, H. Ju, H. S. Cho, B. H. Kim, M. C. Hatzell, J. Kang, S. W. Lee, *Energy Environ. Sci.* **2022**, *15*, 2858; b) H. He, S. Liu, Y. Liu, L. Zhou, H. Wen, R. Shen, H. Zhang, X. Guo, J. Jiang, B. Li, *Green Chem.* **2023**, *25*, 9501.

[9] a) H. Sheng, E. D. Hermes, X. Yang, D. Ying, A. N. Janes, W. Li, J. R. Schmidt, S. Jin, *ACS Catal.* **2019**, *9*, 8433; b) J. Zhu, M. Xiao, Y. Zhang, Z. Jin, Z. Peng, C. Liu, S. Chen, J. Ge, W. Xing, *ACS Catal.* **2016**, *6*, 6335; c) M. Liu, Y. Li, Z. Qi, H. Su, W. Cheng, W. Zhou, H. Zhang, X. Sun, X. Zhang, Y. Xu, Y. Jiang, Q. Liu, S. Wei, *J. Phys. Chem. Lett.* **2021**, *12*, 8706; d) H. Sheng, A. N. Janes, R. D. Ross, D. Kaiman, J. Huang, B. Song, J. R. Schmidt, S. Jin, *Energy Environ. Sci.* **2020**, *13*, 4189.

[10] a) I. Panas, P. Siegbahn, U. Wahlgren, *J. Chem. Phys.* **1989**, *90*, 6791; b) D. C. Ford, A. U. Nilekar, Y. Xu, M. Mavrikakis, *Surf. Sci.* **2010**, *604*, 1565.

[11] a) Z. Cui, Y. Ge, H. Chu, R. Baines, P. Dong, J. Tang, Y. Yang, P. M. Ajayan, M. Ye, J. Shen, *J. Mater. Chem. A* **2017**, *5*, 1595; b) J. Yin, Y. Li, F. Lv, M. Lu, K. Sun, W. Wang, L. Wang, F. Cheng, Y. Li, P. Xi, S. Guo, *Adv. Mater.* **2017**, *29*, 1704681.

[12] X. Zheng, X. Han, Y. Zhang, J. Wang, C. Zhong, Y. Deng, W. Hu, *Nanoscale* **2019**, *11*, 5646.

[13] Z. Zhang, C. Zhao, S. Min, X. Qian, *Electrochim. Acta* **2014**, *144*, 100.

[14] J. Deng, D. Deng, X. Bao, *Adv. Mater.* **2017**, *29*, 1606967.

[15] a) X. Lin, J. Liu, X. Qiu, B. Liu, X. Wang, L. Chen, Y. Qin, *Angew Chem Int Ed Engl* **2023**, *62*, e202306333; b) Z. Wang, Y. Zhou, D. Liu, R. Qi, C. Xia, M. Li, B. You, B. Y. Xia, *Angew Chem Int Ed Engl* **2022**, *61*, e202200552.

[16] L. Tao, Y. Wang, Y. Zou, N. Zhang, Y. Zhang, Y. Wu, Y. Wang, R. Chen, S. Wang, *Adv. Energy Mater.* **2020**, *10*, 1901227.

[17] R. Gao, L. Pan, Z. Li, C. Shi, Y. Yao, X. Zhang, J. J. Zou, *Adv. Funct. Mater.* **2020**, *30*, 1910539.

[18] a) R. Guo, Y. He, R. Wang, J. You, H. Lin, C. Chen, T. Chan, X. Liu, Z. Hu, *Inorg. Chem. Front.* **2020**, *7*, 3627; b) H. Wang, C. Wang, W. Zhang, S. Yao, *Int. J. Hydrogen Energy* **2022**, *47*, 14916.

[19] X. Chu, Y. Liao, L. Wang, J. Li, H. Xu, *Chin. Chem. Lett.* **2023**, *34*, 108285.

[20] B. Qin, Y. Li, H. Wang, G. Yang, Y. Cao, H. Yu, Q. Zhang, H. Liang, F. Peng, *Nano Energy* **2019**, *60*, 43.

[21] a) Y. Wang, H. Yang, Z. Liu, K. Yin, Z. Wang, H. Huang, Y. Liu, Z. Kang, Z. Chen, *J. Energy Chem.* **2023**, *87*, 247; b) Y. Wang, H. Huang, J. Wu, H. Yang, Z. Kang, Y. Liu, Z. Wang, P. W. Menezes, Z. Chen, *Adv. Sci.* **2023**, *10*, 2205347.

[22] a) D. Zhang, Z. Wang, F. Liu, P. Yi, L. Peng, Y. Chen, L. Wei, H. Li, *J. Am. Chem. Soc.* **2024**, *146*, 3210; b) Y. Bu, Y. Wang, G. F. Han, Y. Zhao, X. Ge, F. Li, Z. Zhang, Q. Zhong, J. B. Baek, *Adv. Mater.* **2021**, *33*, 2103266; c) S. Siahrostami, S. J. Villegas, A. H. Bagherzadeh Mostaghimi, S. Back, A. B. Farimani, H. Wang, K. A. Persson, J. Montoya, *ACS Catal.* **2020**, *10*, 7495.